Ⓔ

X-RAY HARDNESS EVOLUTION IN GRB AFTERGLOWS AND FLARES: LATE-TIME GRB ACTIVITY WITHOUT N_H VARIATIONS

NATHANIEL R. BUTLER[1,2] AND DANIEL KOCEVSKI[2]

ABSTRACT

We show that the X-ray and γ-ray spectra of *Swift* GRBs and their afterglows are consistent with the emission characteristic of an expanding, relativistic fireball. The classical afterglow due to the impact of the fireball on the external medium is often not observed until 1 to several hours after the GRB. Focusing on GRBs 061121, 060614, and 060124, but generalizing to the full (>50 Ms XRT exposure) *Swift* sample up to and including GRB 061210, we show that the early emission in >90% of early afterglows has a characteristic νF_ν spectral energy E_{peak}, which likely evolves from the γ-rays through the soft X-ray band on timescales of 10^2–10^4 s after the GRB. The observed spectra are strongly curved when plotted with logarithmic axes and have often been incorrectly fitted in other studies with a time-varying soft X-ray absorption. The spectral evolution inferred from fitting instead models used to fit GRBs demonstrates a common evolution—a power-law hardness-intensity correlation and hard-to-soft evolution—for GRBs and the early X-ray afterglows and X-ray flares. Combined with studies of short-timescale variability, our findings indicate a central engine active for longer than previously suspected. The GRB spectra are observed to become very soft at late times due to an intrinsic spectral evolution and due to the surprising faintness of some afterglows. We discuss models for the early X-ray emission.

Subject headings: gamma rays: bursts — supernovae: general — X-rays: general

Online material: color figures

1. INTRODUCTION

The *Swift* satellite (Gehrels et al. 2004) and its X-ray telescope (Burrows et al. 2005b) have opened a new window into the early lives of γ-ray bursts (GRBs) and their afterglows. We see a complex array of behaviors, many of which appear to be in direct conflict (e.g., O'Brien et al. 2006; Panaitescu et al. 2006; Willingale et al. 2006) with the well-tested internal-external shock GRB and afterglow model (Rees & Mészáros 1994; Sari & Piran 1997; Sari et al. 1998; Wijers & Galama 1999). In this fireball model, the GRB is produced via collisions of shells in a relativistic outflow, and an afterglow arises later, as the ejecta sweep up and heat the surrounding medium. The *Swift* afterglows exhibit dramatic flaring, rapidly decaying prompt emission tails, and typically a broad plateau phase until $t \approx 10^4$ s (e.g., Nousek et al. 2006). Early afterglow observations prior to *Swift* (e.g., Frontera et al. 2000) suggested instead a ~10 s duration burst rapidly gone and replaced by the fading afterglow emission. How these observations are to be reconciled and what mechanisms produce the early afterglow emission are key open questions.

Particularly intriguing, several recent studies fit the *Swift* X-Ray Telescope (XRT) data and infer a time-variable soft X-ray absorption (Starling et al. 2005; Rol et al. 2007; Campana et al. 2007). This would imply that the early afterglow is stripping electrons from a dense shell of light-element–rich material located $R \lesssim 1$ pc from the GRB, which was not already fully ionized by the GRB. It is difficult to detect such an effect because of the strong spectral evolution common in the early afterglows (e.g., Vaughan et al. 2006; Butler 2007a, hereafter Paper I). A changing column density N_H cannot easily be separated from intrinsic afterglow spectral evolution, given the narrow XRT bandpass. If the early

X-ray spectra exhibit log-log curvature like that of GRBs, which have νF_ν spectral turnovers at a characteristic energy E_{peak} (e.g., Preece et al. 2000; Kaneko et al. 2006), then evolution in the curvature could be mistaken for variations in N_H.

As we discuss below, plots of early XRT spectra do show strong log-log curvature and an inferred E_{peak}, which typically passes in time through the X-ray band. This produces a changing X-ray hardness, which we observe to correlate with the flux. A close analogy can be found in the spectral evolution of GRBs observed by the Burst and Transient Source Experiment (BATSE; Fishman et al. 1989). A characteristic feature of these spectra and light curves is a hard-to-soft evolution in time and a power-law hardness-intensity correlation (Golenetskii et al. 1983; Kargatis et al. 1995; Norris et al. 1996; Fenimore et al. 1995, 1996). The recent refined study of Borgonovo & Ryde (2001) measures a power-law relation between the characteristic energy E_{peak} and the bolometric flux F_{bol} valid for >57% of GRB pulses, $E_{peak} \propto F_{bol}^{0.5\pm0.2}$. We observe a consistent correlation in the soft, early-time XRT data.

In Paper I, we present evidence for this outlier population of extremely soft afterglows in the first year of *Swift* XRT afterglow data. Although they were identified via an automated search for spectral lines, the spectra are also well fitted by models containing multiple continuum components. Below and in Butler & Kocevski (2007), we explore further the phenomenology associated with this soft emission. We demonstrate that GRB-like behavior is present in the first $t \lesssim 1$ hour of >90% of the afterglows and is especially prominent during the flaring. In two cases, thanks to Burst Alert Telescope (BAT) triggers on bright precursors, X-ray emission coincident in time with the classical GRB is detected and can be shown to have properties quite similar to the highly time-variable emission at later times. This is strong evidence—to be combined with the short-timescale variability studies (e.g., Burrows et al. 2005a; Falcone et al. 2006; Romano et al. 2006a; Pagani et al. 2006; Kocevski et al. 2007)—relating the flare and early afterglow emission to the GRB central engine.

---

[1] Townes Fellow, Space Sciences Laboratory, University of California, Berkeley, CA 94720-7450.
[2] Department of Astronomy, University of California, Berkeley, CA 94720-3411.

2. DATA REDUCTION

Our automated pipeline at the University of California Berkeley downloads the *Swift* data in nearly real time from the *Swift* Archive[3] and quicklook site. We use the calibration files from the 2006-04-27 BAT and XRT database release. The additional automated processing described below is done uniformly for all afterglows via custom IDL scripts. The final data products are available for general consumption.[4]

The XRT suffers from a significant number of bad or unstable pixels and columns. Two central detector columns were lost due to a micrometeorite strike.[5] For the early afterglows ($t \lesssim 10^3$ s), when the satellite initially points the XRT at the source without the precise localization information needed to offset from the bad columns, a large and time-dependent fraction of the flux can be lost. In order to produce accurate light curves and properly normalized spectra, it is necessary to accurately determine the position centroid and to precisely track the loss of source and background flux due to the bad detector elements on short ($\sim$few seconds) timescales.

2.1. *Photon-counting (PC) Mode Light Curves*

We begin by projecting the data in the $0.5-8.0$ keV band from each PC mode follow-up observation onto a tangent plane centered at the source position quoted by the XRT Team. In raw coordinates, we reject all pixels with more than six counts and also containing more signal than is contained in the surrounding 8 pixels summed. Using the aspect solution file (`*sat*.fits`), we determine the satellite pointing for each detection frame. We then map the bad pixels in raw detector coordinates determined by `xrtpipeline` and by our algorithm onto the sky on a frame-by-frame basis. This is used to generate exposure maps for the full observation and as a function of time.

Using the full exposure map, we determine the afterglow position centroid (see Butler 2007b) to fix the source extraction region. We consider a 16 pixel radius source extraction region, surrounding by an annular background extraction region of outer radius 64 pixels. Running `wavdetect` (see Butler 2007b), we then determine the positions of field sources in the image. We mask out the regions corresponding to the field sources from the source and background extraction regions. Also, using the point-spread function (PSF) model (`swxpsf20010101v003.fits`) at 1.3 keV, we determine the level of residual field source contamination in the source extraction region (typically negligible) for later subtraction.

Initially ignoring pileup, we extract the source and background counts for each good time interval of data acquisition. The fraction of lost signal and the scale factor relating the background in the source and background extraction regions is determined for each extraction using the time-dependent exposure map. Assuming these exposure corrections for the entirety of each time interval, we subdivide the counts in each interval so that a fixed signal-to-noise ratio (S/N) of 3 is achieved.

In order to check and to account for pileup, we perform a coarse Bayesian blocking (Scargle 1998), with a strong prior weight against adding a new segment (e^{-50}). Using the maximum observed count rate in each segment thus determined, we find the minimum aperture necessary to reduce the source signal to levels where pileup is negligible. The coarse blocking results in a small number of regions (typically 2–3) of differing inner

extraction radius for an afterglow. We assume pileup is important for count rates >0.5 counts s^{-1} (see also Nousek et al. 2006). The light curves are verified to transition smoothly across regions of different inner extraction region radius. Using the time intervals and pileup-corrected apertures thus determined, we rebin the data to a S/N of 3 and recalculate the exposure correction for each time interval. The final time regions and exposure corrections define our temporal extractions regions for the extraction of light curves in different energy bands and for the extraction of spectra below.

2.2. *Windowed Timing (WT) Mode Light Curves*

Our reduction of the WT mode data closely parallels our PC mode reduction, except that it is more natural to extract the WT mode data in raw detector coordinates than in sky coordinates, as done above for the PC mode data. This is due to the readout mode; detector pixels are summed in RAW-Y, and the resulting data are in column (RAW-X) format.

Summing the data from each WT mode follow-up, we reject any RAW-X columns containing a count rate >10 σ relative to the background, after first ignoring pixels in the 16 pixel source extraction region. We also reject any RAW-X columns containing 100 times more signal than the highest neighboring column (or >100 if the neighbors contain no signal). Using the sky image determined from the PC mode data and the satellite aspect, we project the background onto the RAW-X axis and form a background mask for the 64 pixel outer radius and 16 pixel inner radius extraction region. We do not allow masking of the pixels within the central 16 pixel source regions. If the source is bright ($>10^3$ counts s^{-1}), we recenter the source and background apertures. Small aspect shifts $\sim$1 pixel are not uncommon between the PC and WT mode data and must be accounted for.

We determine the exposure corrections as for the PC mode data, but also adjusting the PSF model for the WT mode summing of RAW-Y pixels. We note that our exposure corrections account for source signal contained in the background region. We determine a pileup correction as above, but with a limiting source count rate of 150 counts s^{-1} (see also Nousek et al. 2006).

2.3. *PC and WT Mode Spectra*

Spectral response files are generated using the `xrtmkarf` task for each time interval of interest. Our invocation of the task ignores the exposure maps calculated above, determining the energy dependence of the source extraction and assuming only the inner and outer source and background regions. We then adjust the normalization of the resulting ancillary response file (ARF) to account for the actual loss in flux ($0.5-8.0$ keV) on a pixel-by-pixel basis using the divided time intervals and associated exposure corrections determined above. The spectra are fit in ISIS.[6] For each spectral bin, we require a S/N of 3.5. We define S/N as the background-subtracted number of counts divided by the square root of the sum of the signal counts and the variance in the background. As done in Paper I, we restrict our attention to time-resolved spectra containing 500 or more counts or to spectra formed by grouping two or more of the 500 count spectra.

We fit the PC and WT mode data over the $0.3-10.0$ keV range, also accounting for the systematic calibration uncertainties, $\sim$3%.[7] In WT mode, we allow the detector gain to vary by ± 80 eV.[8]

---

[3] See ftp://legacy.gsfc.nasa.gov/swift/data.

[4] See http://astro.berkeley.edu/~nat/swift.

[5] See http://swift.gsfc.nasa.gov/docs/heasarc/caldb/swift/docs/xrt/SWIFT-XRT-CALDB-01_v5.pdf.

[6] See http://space.mit.edu/CXC/ISIS.

[7] See http://swift.gsfc.nasa.gov/docs/heasarc/caldb/swift/docs/xrt/spie05_romano.pdf.

[8] See http://swift.gsfc.nasa.gov/docs/heasarc/caldb/swift/docs/xrt/xrt_bias.pdf.

2.4. *BAT Light Curves and Spectra*

We establish the energy scale and mask weighting for the BAT data by running the `bateconvert` and `batmaskwtevt` tasks. The mask-weighting removes flux from background sources. Spectra and light curves are extracted with the `batbinevt` task, and response matrices are produced by running `batdrmgen`. We apply the systematic error corrections to the low-energy BAT spectral data, as suggested by the BAT Digest Web site,[9] and fit the data using ISIS. The spectral normalizations are corrected for satellite slews using the `batupdatephakw` task. For GRB 060124 below, BAT spectral fits are performed on the mask-tagged light-curve data in four channels, assuming the on-axis response and also accounting for the systematic error.

3. THE JOINT BAT+XRT SPECTRA OF THREE EVENTS

There are two bright events in the XRT sample that overlap in time entirely with what would commonly be thought of as the prompt phase of GRB emission. The observations by the XRT were made possible by a bright precursor just minutes prior to each GRB observed in the BAT, on which the BAT triggered. We therefore have both BAT and XRT data for each event, GRB 060124 and GRB 061121. We also discuss the bright event GRB 060614, which has excellent XRT coverage due to an early, rapid spacecraft slew.

Figure 1 displays spectral fits to a selected set of time-resolved intervals in each event. The best-fit model parameters are given in Table 1. The time evolution of these parameters are presented and discussed in detail in the next three subsections.

3.1. *GRB 060124*

Swift BAT triggered and located the precursor to GRB 060124, allowing the XRT to slew and begin simultaneous observations 106 s later (Holland et al. 2006). This event is also discussed in Romano et al. (2006b). The 0.3–10.0 keV light curve is plotted in Figure 2. There are two prominent peaks. As shown in the background (*lighter two shades of gray*), the time profile in the soft XRT channel (0.3–1.3 keV) is broader than that in the hard channel (1.3–10.0 keV). The BAT light curve shows even narrower time structure and resolves the broad first XRT peak into at least three subpeaks. The light curve after the flare ($t > 10^4$ s) and extending to 22 days is well fit by a power law $t^{-1.32\pm0.01}$ ($\chi^2/\nu = 535.2/465$).

We group the XRT data into $\gtrsim 500$ counts spectra and fit power laws (Fig. 3, *left*). Each fit is statistically acceptable, with a reduced χ^2 of order unity. The photon index Γ is observed to decrease in time, although with modulation in time that correlates with the X-ray flux and with $N_{\rm H}$ (see explanation in § 5.1). At late times ($t > 10^4$ s), the $N_{\rm H}$ values asymptotically approach the blue dashed curve [$N_{\rm H} = (2.3 \pm 0.2) \times 10^{21}$ cm^{-2}] plotted in the figure.

To study the time-varying log-log curvature, we jointly fit the BAT and XRT data using the Band et al. (1993) model. Here we choose extraction regions that allow for a BAT S/N of 20 or higher. We also fix the column density $N_{\rm H}$ to the late-time value. The model fit is actually a progression of fits of nested models (e.g., Protassov et al. 2002), from the simplest power-law model to a power law times exponential model, to the smoothly broken power-law Band model. Each more complex model has one additional degree of freedom. We accept or reject the more complex model at each stage by requiring $\Delta\chi^2 > 2.706$ (i.e., 90% con-
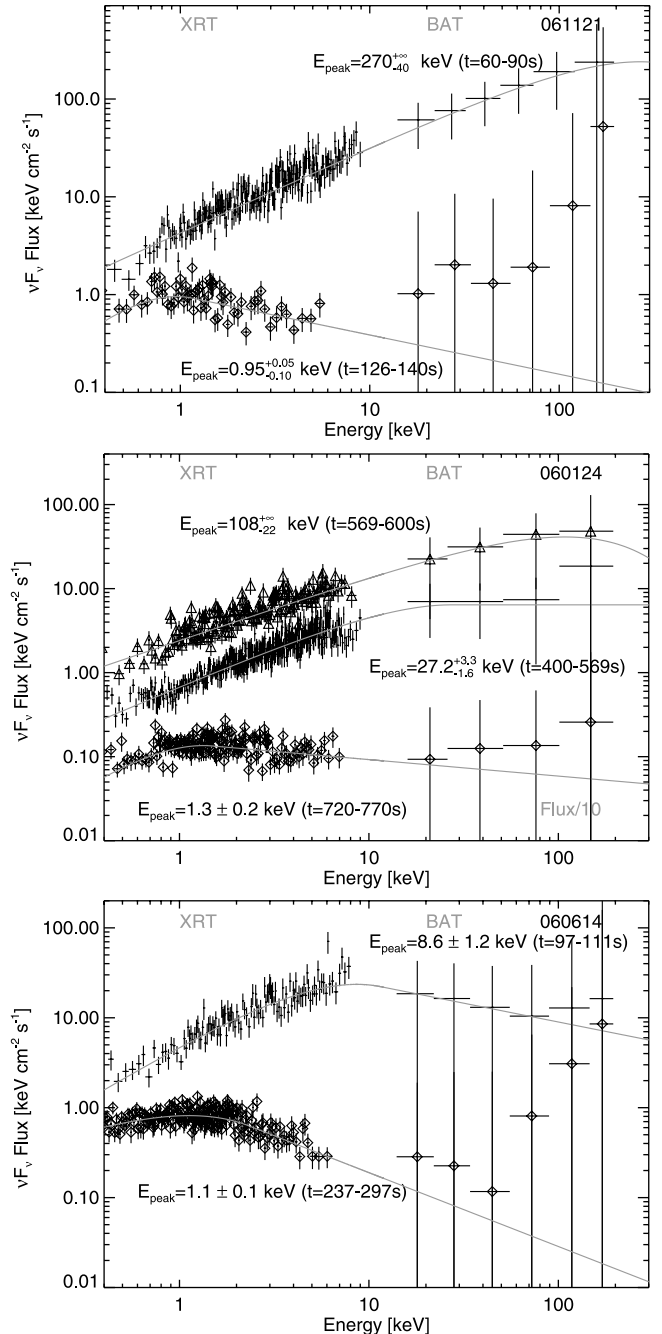
9 See http://swift.gsfc.nasa.gov/docs/swift/analysis/bat_digest.html.

Fig. 1.—Selected νF_ν spectra from GRBs 061121, 060124, and 060614, demonstrating the Band model fits to a time-varying spectral curvature—as seen in plots with logarithmic axes—and $E_{\rm peak}$ evolution. The X-ray data are corrected for photoelectric absorption using the best-fit late-time values of $N_{\rm H}$ in Fig. 3 (*left*). The softest spectrum in the middle panel is divided by a factor of 10 for legibility. The counts spectra are jointly fit by forward-folding the Band model through the instrument response matrices. For the spectral fits (Table 1), the BAT data are not binned as shown here. [*See the electronic edition of the Journal for a color version of this figure.*]

fidence). If the data are acceptably fit by only the power-law model, we quote a limit on $E_{\rm peak}$ using either the exponential times power-law model (for $\Gamma < 2$) or the constrained Band formalism (Sakamoto et al. 2004; for $\Gamma > 2$). In order that $E_{\rm peak}$ correspond to a peak in the νF_ν spectrum, we require the low energy index $\alpha > -2$ and the high energy index $\beta < -2$. After finding that the fits were consistent with $\alpha < 0$, as also found for BATSE GRBs (Preece et al. 2000; Kaneko et al. 2006), we

TABLE 1
Selected Band or Power Law Times Exponential Model Spectral Fits

GRB	Time (s)	α	β	$E_{\rm peak}$ (keV)	0.3–10 keV Flux (10^{-9} ergs cm^{-2} s^{-1})	χ_ν^2 (ν)	Significance
060124........................	569–600	-1.23 ± 0.04	. . .	$108^{+\infty}_{-22}$	26.8 ± 1.0	1.21 (154)	5.9 σ
060124........................	400–569	-1.04 ± 0.03	$-2.0^{+0.0}_{-0.1}$	$27.2^{+3.3}_{-1.6}$	$8.6^{+0.2}_{-0.1}$	1.01 (410)	10^{-77}
060124........................	720–770	$-0.3^{+0.3}_{-0.6}$	-2.2 ± 0.1	1.3 ± 0.2	$5.8^{+0.3}_{-0.2}$	1.08 (158)	10^{-12}
061121........................	60–90	$-1.12^{+0.01}_{-0.02}$	. . .	$270^{+\infty}_{-40}$	$55.3^{+1.0}_{-1.3}$	1.07 (270)	9.3 σ
061121........................	126–140	$-0.0^{+0.0}_{-0.9}$	$-2.4^{+0.1}_{-0.2}$	$0.95^{+0.05}_{-1.0}$	3.7 ± 0.2	1.16 (117)	3.9 σ
060614........................	97–111	-0.7 ± 0.1	-2.4 ± 0.1	8.6 ± 1.2	59^{+3}_{-2}	0.86 (169)	10^{-98}
060614........................	237–297	-1.2 ± 0.2	$-2.8^{+0.2}_{-0.3}$	1.1 ± 0.1	3.2 ± 0.1	0.97 (246)	10^{-27}

Notes.—The quoted errors correspond to the 90% confidence region. The "Significance" column refers to the fit improvement significance relative to a simple power-law model, determined from a $\Delta\chi^2$ test. The quoted fluxes are unabsorbed.

included this as a constraint to derive the tightest error bounds on the other model parameters.

As shown in Figure 3 (*right*), the data are better fit (>90% confidence) with the Band model in most of the time regions. The peak energy rises and declines with each of the four prominent light-curve pulses. For each pulse, we present power-law fits to the $E_{\rm peak}$ declines. The rises are not well measured, as is also typically the case for BATSE bursts (e.g., Kocevski et al. 2003). Prior to $t \lesssim 800$ s, the observed spectrum corresponds mostly to the low-energy portion of the Band model spectrum, except episodically at the flare troughs, where $E_{\rm peak}$ enters the X-ray band. These times regions are also those of highest $N_{\rm H}$ in Figure 3 (*left*). The third pulse decline exhibits a strong evolution in both α and $E_{\rm peak}$. After $t \sim 800$ s the observed spectrum corresponds to the high-energy portion of the model spectrum, and $E_{\rm peak}$ has transited the X-ray band. Figure 1 (*middle*) plots the νF_ν spectrum at three time epochs.

Motivated by the watershed event GRB 060218 (Paper I; Campana et al. 2006a), we also attempt to fit the X-ray curvature using a power-law plus blackbody model. The fits to the X-ray data alone are provocative and show a smooth temperature decline after each of the two major pulses. However, the fits are statistically unacceptable when we also attempt to account for the BAT data. This is also true for the GRB 061121 spectra discussed in § 3.2. This should be taken as a caveat also to the power-law

plus blackbody fits presented for the XRT data in Paper I, where the derived blackbody temperature variation may apply instead to $E_{\rm peak}$ variations. We note, however, that the X-ray spectra of the unusual GRB 060218 burst and afterglow are better fit by a blackbody plus power law than by a Band model (Paper I). We do not consider the possibility of two power laws and a blackbody for the bursts discussed here.

3.2. GRB 061121

Swift BAT triggered on and began observing the precursor to GRB 061121 55 s prior to the XRT slew toward and onset of the main GRB event (Page et al. 2006). The *Swift* team designated this event a "Burst of Interest" (Gehrels et al. 2006) due to the rare simultaneous detections in the BAT and XRT bands and at longer wavelengths. As shown in Figure 4, the γ-ray and X-ray light curves show multiple peaks, with most of the prominent time structure apparent in only the γ-ray band.

In Figure 3 (*top*), we show the results of power-law and Band model fits to the 061121 data. The data do not have as high S/N in the X-ray band as the 060124 data; however, many of the same trends are apparent. There is a hard-to-soft evolution apparent in the power-law photon index and a correlation between the photon index and $N_{\rm H}$. The Band model photon index goes from the low-energy side to the high-energy side once $E_{\rm peak}$ has crossed the X-ray band. $E_{\rm peak}$ also appears to rise and fall with flaring prior to 80 s. The νF_ν spectrum is plotted at two epoch in Figure 1 (*top*). For the Band fits, we use the late-time ($t > 10^4$ s) $N_{\rm H} = (2.5 \pm 0.3) \times 10^{21}$ cm^{-2}.

XMM-Newton data for this event beginning after $t \approx 6$ hr show consistent power-law fits with our late-time fits (Page et al. 2007). In particular, $N_{\rm H} = 1.71^{+0.03}_{-0.02} \times 10^{21}$ cm^{-2}, consistent with our late-time $N_{\rm H}$ at the 2 σ level and well below the mean early-time value. *XMM-Newton* and XRT data generally agree well with respect to the late-time $N_{\rm H}$ determinations (e.g., Moreti et al. 2006).

3.3. GRB 060614

The GRB 060614 (Parsons et al. 2006) afterglow fades rapidly as a power law from the prompt emission, with no flaring (Fig. 5). There is excellent BAT+XRT coverage during the prompt tail emission lasting to $t \sim 150$ s. We observe weak $N_{\rm H}$-Γ- correlated modulations during the rapidly fading tail, which would imply an $N_{\rm H}$ that decreases in time, reaching the value marked by the dashed line in Figure 3 (*left*) by $t = 10^4$ s.

However, the Band model fits show an $E_{\rm peak}$ that passes through the X-ray band without requiring a varying $N_{\rm H}$. Extrapolating backward through the prompt emission, the best-fit decay also fits two $E_{\rm peak}$ limits derived for the BAT-only prompt
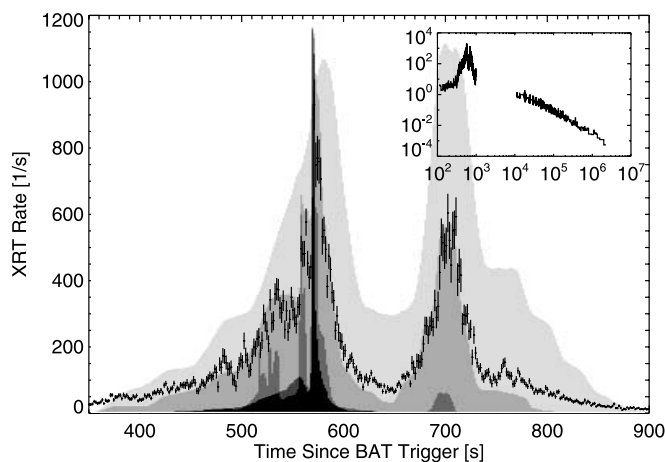

Fig. 2.—Light curve for GRB 060124. The X-ray data (0.3–10.0 keV) are plotted in black. The shaded regions in the background depict the X-ray light curves in two energy bands (0.3–1.3 keV and 1.3–10.0 keV) and in the hard X-ray/γ-ray bands of BAT (15–100 keV and 100–350 keV). The background light curves are each denoised and normalized to their peak intensity. The harder regions are darker. The subpanel shows the early and late XRT light curve.
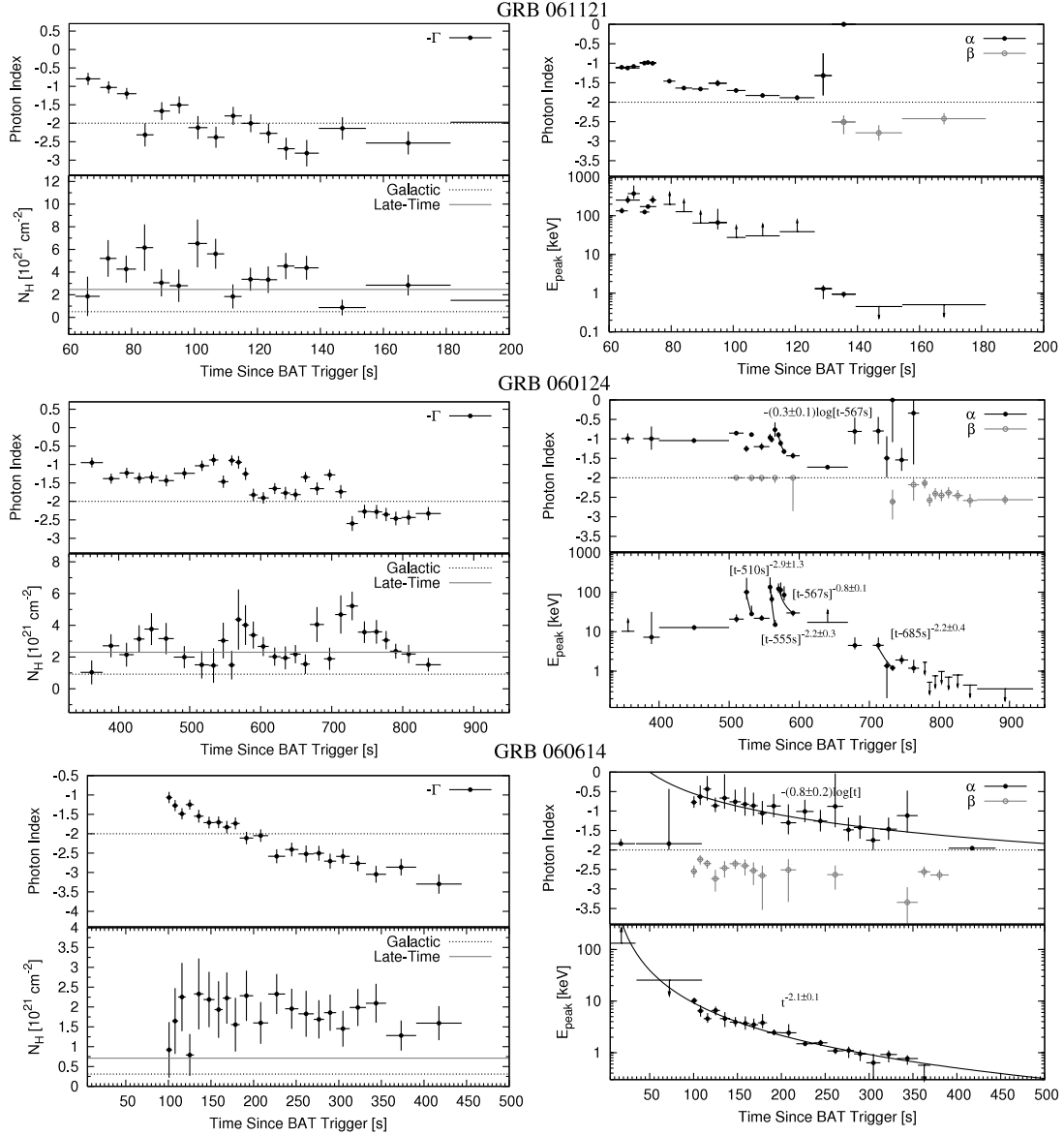
FIG. 3.—Power-law (*left*) and Band model (*right*) fits to the GRBs 061121, 060124, and 060614. Time-correlated $N_H - \Gamma$ variations in the left plots are better modeled by spectral models with time-evolving E_{peak} in the right plots. The N_H values peak when $E_{peak} \approx 1$ keV. The power-law fits are performed for only the X-ray data, whereas the Band fits (actually nested power law, then exponential times power law, then Band fits, as described in the text) apply to the X-ray and γ-ray data. Trends in the Band model parameters, when observed, are fitted and presented in Table 3 and in the text. These time variations are given relative to the approximate pulse start times. Galactic column densities are taken from Dickey & Lockman (1990) The Band fits use the late-time N_H values plotted in the left panels, derived from X-ray fits at $t > 10^4$ s. [*See the electronic edition of the Journal for a color version of this figure.*]

emission. Figure 1 (*bottom*) plots the νF_ν spectrum at two epochs. Expressed in terms of the flux F_{XRT} as measured by the XRT rate, $E_{peak} \propto F_{XRT}^{-0.72\pm0.03}$. The low-energy photon index α also appears to evolve in time after the main GRB emission.

3.4. *Hardness Plots for GRBs 061121, 060124, and 060614*

It will be useful below to see how the spectral evolution in the early X-ray light curves of GRBs 061121, 060124, and 060614 impacts the X-ray hardness ratio. We define this as the ratio of counts in the 1.3–10.0 keV band to the counts in the 0.1–1.3 keV band. The average hardness ratio (HR) for most afterglows is 1.

Figure 6, in nine panels, shows the hardness and rate time profiles for GRBs 061121, 060124, and 060614. The middle panels (*top to bottom*) show the X-ray light-curve fit using an extension of the Bayesian blocks algorithm (Scargle 1998) to piecewise logarithmic data. The rate and hardness data are fit jointly, allowing the minimum number of power-law segments such that

$\chi^2/\nu \sim 1$. The fits to the rate and hardness are plotted in the top and middle panels, indexed according to time. The hardness tracks the flux and moves along roughly parallel tracks. In the bottom panels, the flux in both XRT bands (*top*) and the hardness (*bottom*) are plotted for each power-law segment. During the decline phase of each pulse, the hardness scales as the square root of the rate for GRBs 061121 and 060124. For GRB 060614, the hardness and flux track as found above for E_{peak} and flux.

Each pulse in GRB 060124 peaks at roughly the same time, independent of energy band. There is, however, a hardness rise during the flux rise because the hard band increases more rapidly. There is also a modest overall hard-to-soft trend throughout the light curve.

The hardness plot does not capture the strong spectral variations between 500 and 600 s in GRB 060124, which are apparent from the broadband fits (Fig. 3, *middle*) and occur mostly for E_{peak} above the XRT bandpass. The time dependences of E_{peak}
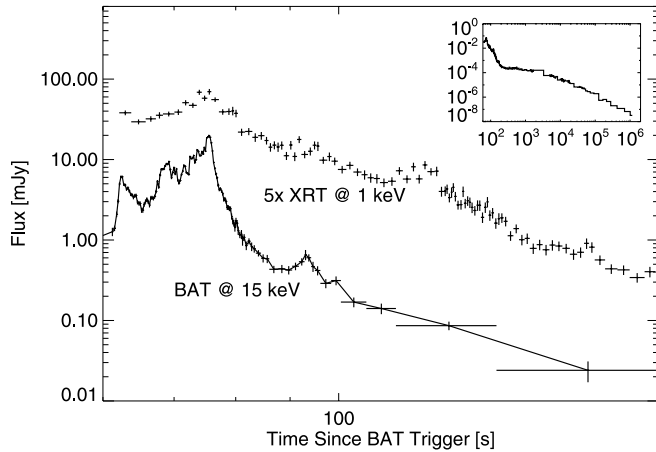
FIG. 4.—Hard X-ray BAT and XRT light curves for GRB 061121. The late-time light curve (a plateau at $t \sim 200$ s followed by a decline beginning at $t \sim 3000$ s) is plotted in the subpanel. The XRT light curve has been multiplied by 5 to bring it above the BAT light curve.
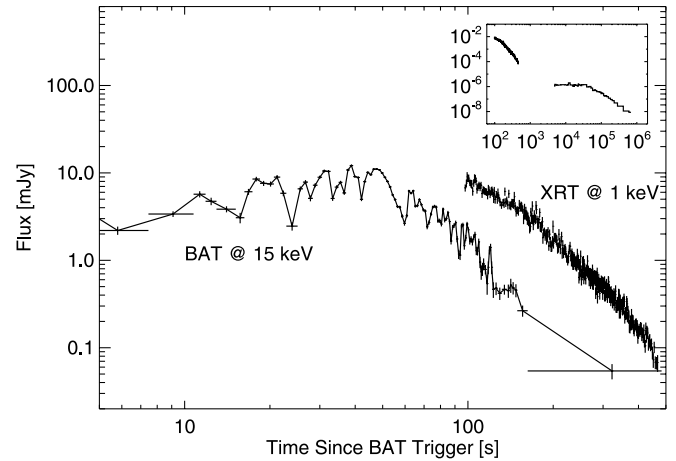

FIG. 5.—Hard X-ray BAT and XRT light curves for GRB 060614. The late-time light curve (a plateau at $t \sim 200$ s followed by a decline beginning at $t \sim 4000$ s) is plotted in the subpanel.

during this region and later are given in the figure. The E_{peak} dependence can also be given in terms of the flux F, in order to sidestep the problem of unknown start time. For all but the last flare, where we use the XRT count rate, we use the BAT $15-350$ keV count rate for the flux. For pulses $1-4$, we find $E_{\mathrm{peak}} \propto F_{\mathrm{BAT}}^{-3.6 \pm 1.7}$, $F_{\mathrm{BAT}}^{-1.8 \pm 0.5}$, $F_{\mathrm{BAT}}^{-0.3 \pm 0.1}$, and $F_{\mathrm{XRT}}^{-1.2 \pm 0.2}$, respectively. In the bottom right and left panels of Figure 6, we show that the hardness can be described by the square root of the observed flux, as is common for GRBs at higher energies observed with BATSE (e.g., Borgonovo & Ryde 2001; Ryde & Petrosian 2002; Kocevski et al. 2003; Ryde 2005; § 5).

For GRB 061121, the hardness plots show an initial hardening followed by a decrease in the hardness, which scales well with the square root of the X-ray rate. There may be broad pulses on top of the decline, although these have only a minor impact on the hardness. GRB 060614 appears to exhibit a mostly secular decline in both flux and hardness, corresponding to the fading tail of the prompt emission.

For each GRB, the hardness plot captures the E_{peak} evolution in general terms. Both HR and E_{peak} decrease during rate declines at a similar power of the rate. It is apparently not possible to cleanly if at all separate evolution of α from evolution of E_{peak}, given the hardness alone. From Figure 3 (top and middle right) and also from time-resolved spectral studies of many GRBs (§ 5), these parameters tend to evolve simultaneously.

4. EXAMPLE SPECTRA FOR FOUR OTHER EARLY AFTERGLOWS

Most early X-ray afterglows have a low S/N or no coincident detection by BAT. It is possible to derive E_{peak} values or limits for these early on, given the BAT data. Late-time E_{peak} from the X-ray data typically show values in or passing through the XRT band after 1 to several minutes. The spectral evolution from one such event, GRB 060714 (Krimm et al. 2006), is shown in Figure 7.

The hardness plot (Fig. 7, middle) allows for a finer time sampling of the spectra evolution. The hardness (likely also E_{peak}) rises and declines with the flux along the same track in the hardness rate plane as two flares take place. The column density (not plotted) is a factor of 2 larger in the time interval $140-170$ s than outside that interval, indicating an E_{peak} passage. There are a handful of examples with higher S/N XRT observations.

The GRB 060526 (Campana et al. 2006b) afterglow exhibits time-correlated Γ-N_{H} variations and a corresponding rapid, then

smooth, decline of E_{peak} through the XRT band (Fig. 8, left). The initial GRB pulse ($t < 9.4$ s) is well fit by a simple power law ($\alpha = -1.6 \pm 0.2$, $\chi^2/\nu = 16.83/16$), and we derive $E_{\mathrm{peak}} > 80$ keV (90% confidence). The flare at $t \sim 250$ s is detected by the BAT as well, and we use the BAT data to obtain the best Band model fits. The Band model photon indices are poorly measured. The composite flare and decline is shown in Figure 9. The hardness evolves similarly to the best-fit E_{peak} values.

The very bright afterglow to GRB 060729 (Grupe et al. 2006a) continues to be detected 4.5 months after the GRB. The GRB is over and done with by $t \sim 130$ s in the BAT. We find $E_{\mathrm{peak}} > 50$ keV (90% confidence). After $t > 100$ s in the XRT, there is a rapid decline, interrupted by a flare or rise at 160 s (Fig. 9). Time-correlated N_{H}-Γ variations and an E_{peak} passage through the X-ray band are similar to those discussed above (Fig. 8). We observe that E_{peak} declines with the X-ray rate as $F_{\mathrm{XRT}}^{-0.4 \pm 0.1}$, both before and after the mild flare at $t \sim 180$ s. There is also a possibly significant decline in β with time.

The hardness declines by an order of magnitude, reaching a minimum at $t \sim 250$ s, and then increases to the late-time ($t > 10^3$ s) value. Note that no clear coincident change is present in the rate plot. The hardness plot demonstrates that the late-time emission is spectrally different from the early emission and that its onset occurs at $t \sim 250$ s.

Modest but clear N_{H}-Γ variations are seen for GRB 060904B (Grupe et al. 2006b). The prompt emission ($t < 8.3$ s) has $E_{\mathrm{peak}} = 125^{+135}_{-30}$ keV. E_{peak} transits the X-ray band nicely (Fig. 8). The hardness evolution shows the usual time dependence in the declining tail of the flare (Fig. 9). E_{peak} decays versus the rate as $F_{\mathrm{XRT}}^{-0.7 \pm 0.2}$.

The emission for GRB 060929 (Markwardt et al. 2006) at $t < 13$ s exhibited $E_{\mathrm{peak}} > 75$ keV. The X-ray flare peaking at $t \sim 550$ s is weakly detected by the BAT. In the XRT, there is a clear softening trend (Fig. 9), likely N_{H}-Γ variations, and an E_{peak} declining through the X-ray range (Fig. 8). E_{peak} drops with the X-ray rate as $F_{\mathrm{XRT}}^{-0.6 \pm 0.1}$. The hardness reaches a minimum at $t = 630 \pm 10$ s.

5. DISCUSSION

5.1. Global Sample Properties

In terms of the spectral evolution properties, we see no apparent difference between the fading tales of flarelike X-ray emission and the rapid X-ray declines often observed in trail flaring in
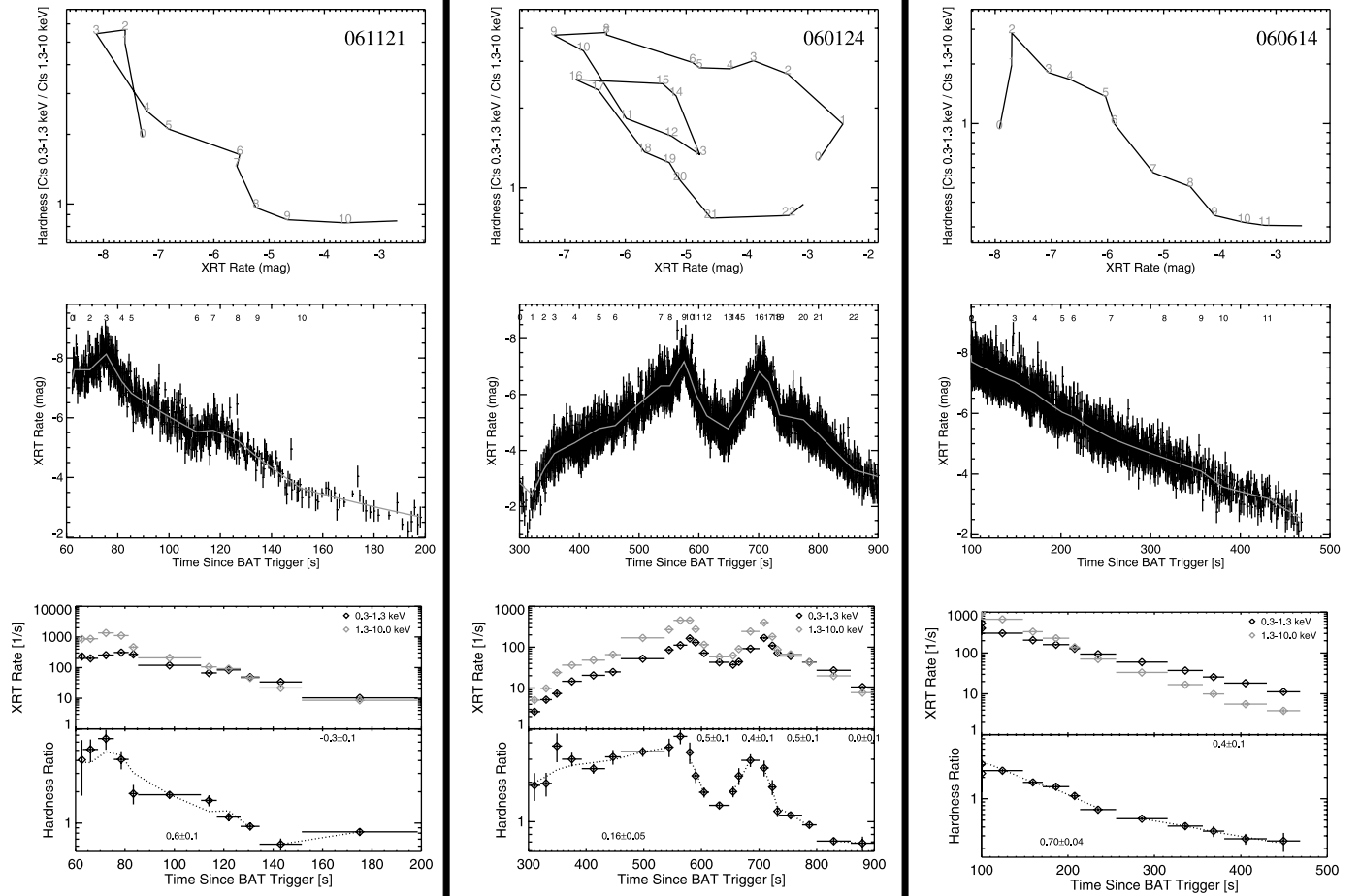
Fig. 6.—*Top*: Hardness evolution in GRBs 061121, 060124, and 060614. *Middle*: Hardness vs. rate fit, indexed as a function of time, showing evolution along roughly parallel tracks. *Bottom*: X-ray light curve and fit as source of the time indexing. The X-ray light curve in each band for each time segment and the hardness during each time segment are shown. This is well fit during the declines by the square root of the rate in GRBs 061121 and 060124 and by a power close to the square root of the rate for GRB 060614. [*See the electronic edition of the Journal for a color version of this figure.*]

BAT (e.g., Tagliaferri et al. 2005; Barthelmy et al. 2005; Cusumano et al. 2006; Vaughan et al. 2006). Indeed, based solely on timing properties, many of the rapid declines also appear to have superimposed flaring (e.g., 060729, Fig. 9; 061121, Fig. 6). The rapid declines are thought to be the fading tail of the prompt emission (Panaitescu et al. 2006; Yamazaki et al. 2006; Lazzati & Begelman 2006; Zhang et al. 2006a), and the X-ray flares are thought to be due to later central engine activity (Zhang et al. 2006a; Ioka et al. 2005; Fan & Wei 2005). We observe clear distinctions between the spectra measured before the light-curve plateau and those after the start of the plateau; only the late spectra exhibit a tight clustering with $\Gamma \approx 2$ (Fig. 10; Paper I; Butler & Kocevski 2007).

Figure 11 shows what we expect to measure from power-law fits to a time-evolving Band model spectrum. As E_{peak} enters the X-ray band, the spectral curvature as would be seen on a plot with logarithmic axes increases, and the inferred X-ray column density increases linearly with an increasing inferred photon index Γ. This occurs despite the fact that only E_{peak} changes in the simulation. Figure 12 suggests that this effect is common in the XRT data (§ 5.2). Figure 13 (*left*) shows that the flares (Table 2) and rapid X-ray declines exhibit significant hardness-intensity and hardness-fluence correlations that closely match the correlations observed for GRBs (§ 5.3 below).

For GRBs it is common to observe finer time structure at higher energies as compared to low energies (Norris et al. 1996;

Fenimore et al. 1995, 1996). Pulses tend to be narrower, fade more rapidly, and evolve stronger spectrally at high energies. Consistent with this, the X-ray flares (and also the rapid declines) appear longer ($8\% \pm 1\%$, on average; Fig. 14, *left*) and with smoother time structure (e.g., Fig. 2) at softer energies. This can be understood as the effect of E_{peak} evolving into the X-ray band, which allows the X-ray emission to be observed longer (e.g., Kocevski et al. 2003; § 5.4). Although it is difficult to see by eye, there is also evidence for a $25\% \pm 5\%$ increase in the flare rise time with decreasing X-ray energy band (Fig. 14, *right*). This is close to the expected pulse-broadening fraction from an extrapolation of the GRB behavior, $1 - (1.3/0.5)^{-0.4} \approx 30\%$, where 0.5 and 1.3 keV are used as approximate lower bandpass energies. Given the possibility that resolved γ-ray flares are blurred together in the X-ray band (e.g., Fig. 2), however, it is not clear how meaningful this apparent consistency is.

5.2. *The Physical X-Ray Column Density Does Not Vary*

The time-resolved XRT afterglows are well fit by absorbed power laws at all epochs (see also Paper I). Prior to a characteristic hardness variation turnoff time $T_{\text{H}} \approx 10^{2}-10^{4}$s, which we discuss for a large sample of bursts in Butler & Kocevski (2007), there is strong evolution in both the best-fit photon indices and the best-fit column densities N_{H}. After this time, the quantities typically do not vary. To fit more complicated models to the early-time afterglows, we have found it necessary to jointly fit
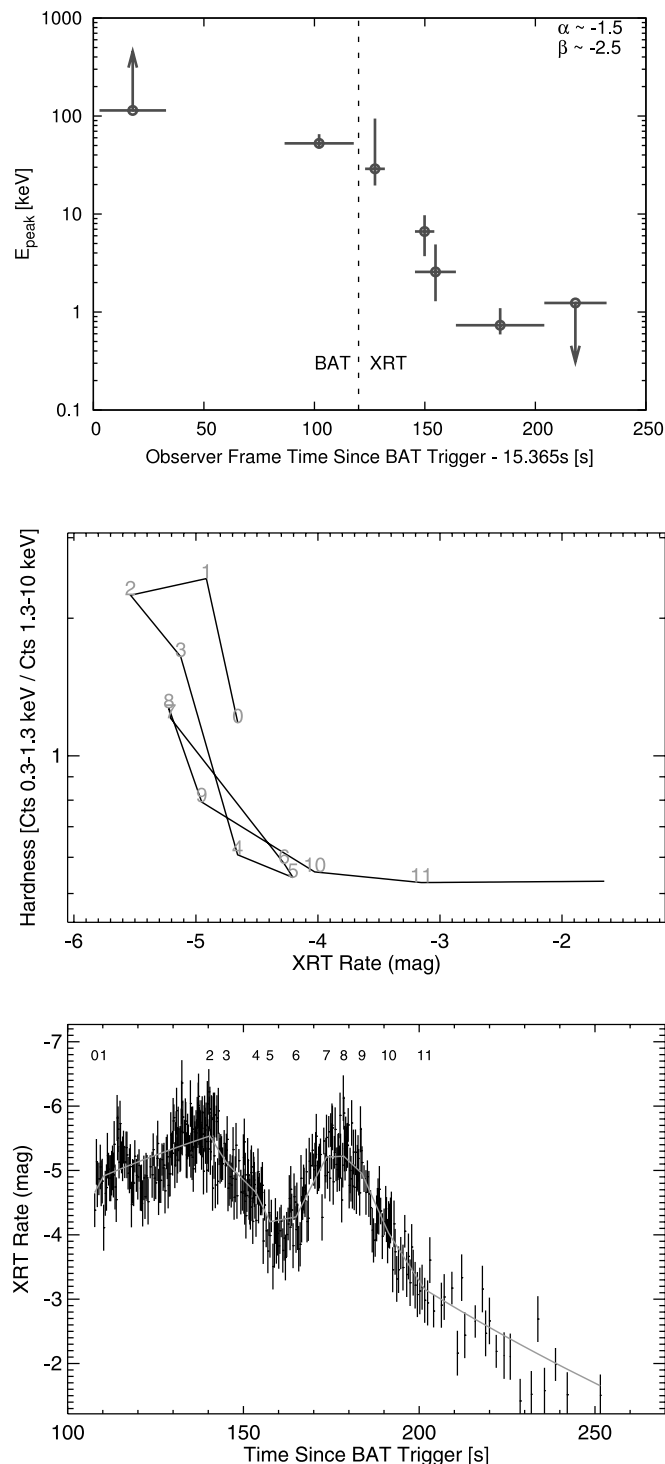
FIG. 7.—Plots of the hardness and E_{peak} evolution for flares after GRB 060714. The Band fits allow only a coarse time resolution, whereas the hardness study demonstrates fine-timescale changes in the spectrum, which track the flux across flares. *Top*: E_{peak} evolution from Band model fits to the BAT and XRT data). *Middle and bottom*: Typical values for the photon indices (α and β) are given. Hardness vs. rate fit, indexed as a function of time, showing parallel evolution tracks. [*See the electronic edition of the Journal for a color version of this figure.*]

the BAT and XRT data (when possible) and to relate the column density to the value measured at late time. The late-time value is typically not the Galactic value.

Band model fits are able to account for both the BAT and XRT emission without a time-variable column density (see also Falcone

et al. 2006). The ubiquitous hardness evolution appears to be best understood in terms of an evolving E_{peak}, as we discuss in detail below.

Several studies have recently claimed a decreasing N_{H}, based on fits to the XRT data (Starling et al. 2005; Rol et al. 2007; Campana et al. 2007; GRBs 050730, 050716, and 050904, respectively). Each study presents a coarsely time-resolved set of spectral fits, which demonstrate a higher N_{H} at early times. This is an artificial feature that we observe in fits to most *Swift* early afterglows. It is especially clear in the brightest afterglows, which often sample the declining tail of the prompt emission. For each of the three bursts with claimed N_{H} variations (e.g., Fig. 15), a fine-timescale spectral analysis reveals an N_{H} that both increases and decreases in time (following Γ and the flux). Observed drops in $N_{H} \gtrsim 10^{21}$ cm^{-2} (or $\gtrsim 10^{22}$ cm^{-2} in the rest frame) on timescales of $10-100$ s are challenging enough, but drops and increases and drops again on these timescales are unphysical.

We strongly caution against taking the early N_{H} values at face value. Measurements of N_{H} at $t \lesssim 10^4$ s will be artificially high. Also, although we cannot rule variations out in all cases, they are not required by the data, and they are also not the simplest interpretation of the data. Firm measurements of N_{H} variability will require finely time-sampled broadband data (e.g., ultraviolet, X-ray, and γ-ray data) to disentangle the effects of the evolving Band model spectrum from the soft X-ray photoelectric absorption.

For those fitting XRT spectra, we recommend measuring N_{H} at late times ($t \gtrsim 10^4$ s) or performing joint fits at different time intervals with a single N_{H} parameter shared between multiple spectra. Jointly fit with BAT when possible. Fine time resolution is essential when testing variable N_{H}; it is not sufficient to fit exponential times power-law models or Band models (e.g., Rol et al. 2007; Campana et al. 2007) with coarse time resolution. The hardness ratio can be utilized to diagnose cases in which inferred N_{H} values are likely to vary artificially.

5.3. *Is the Early XRT Emission the Same as Prompt GRB Emission?*

We have shown for seven events that the early X-ray spectra require a fit model that also has been shown to reliably fit all GRBs (e.g., Preece et al. 2000; Kaneko et al. 2006; Frontera et al. 2000; Sakamoto et al. 2004). The need for such a model is also clear from hardness variations (see also Butler & Kocevski 2007) and time-correlated N_{H}-Γ variations observed for even low S/N afterglows, which demonstrate a characteristic increase in spectral curvature in the XRT band.

In cases where E_{peak} is well measured, or using HR when E_{peak} is poorly measured, we observe a hard-to-soft evolution and a strong hardness-intensity correlation, also commonly seen in GRB pulses. Our correlation can be described as a hardness that tracks the flux to a power 0.43 ± 0.07. From the Band model fits, our best-fit E_{peak}-F relation is 0.7 ± 0.2 (Table 3). A closely consistent power-law relation exists for most GRB pulses, also with a large scatter in observed values (Golenetskii et al. 1983; Kargatis et al. 1995). The scatter is apparently minimized for bolometric measures of flux (Borgonovo & Ryde 2001), yielding $E_{peak} \propto F_{bol}^{0.5\pm0.2}$. The fact that we have observed a consistent relation can be turned around to imply GRB-like emission with $E_{peak} \approx 1$ keV, typically. That *Swift* observes bright X-ray flares appears to be a consequence of this and also due to the surprising fact that the afterglow is faint at these times. It is interesting to speculate that there may be bright optical flares due to internal shocks several hours after some GRBs with faint afterglows.
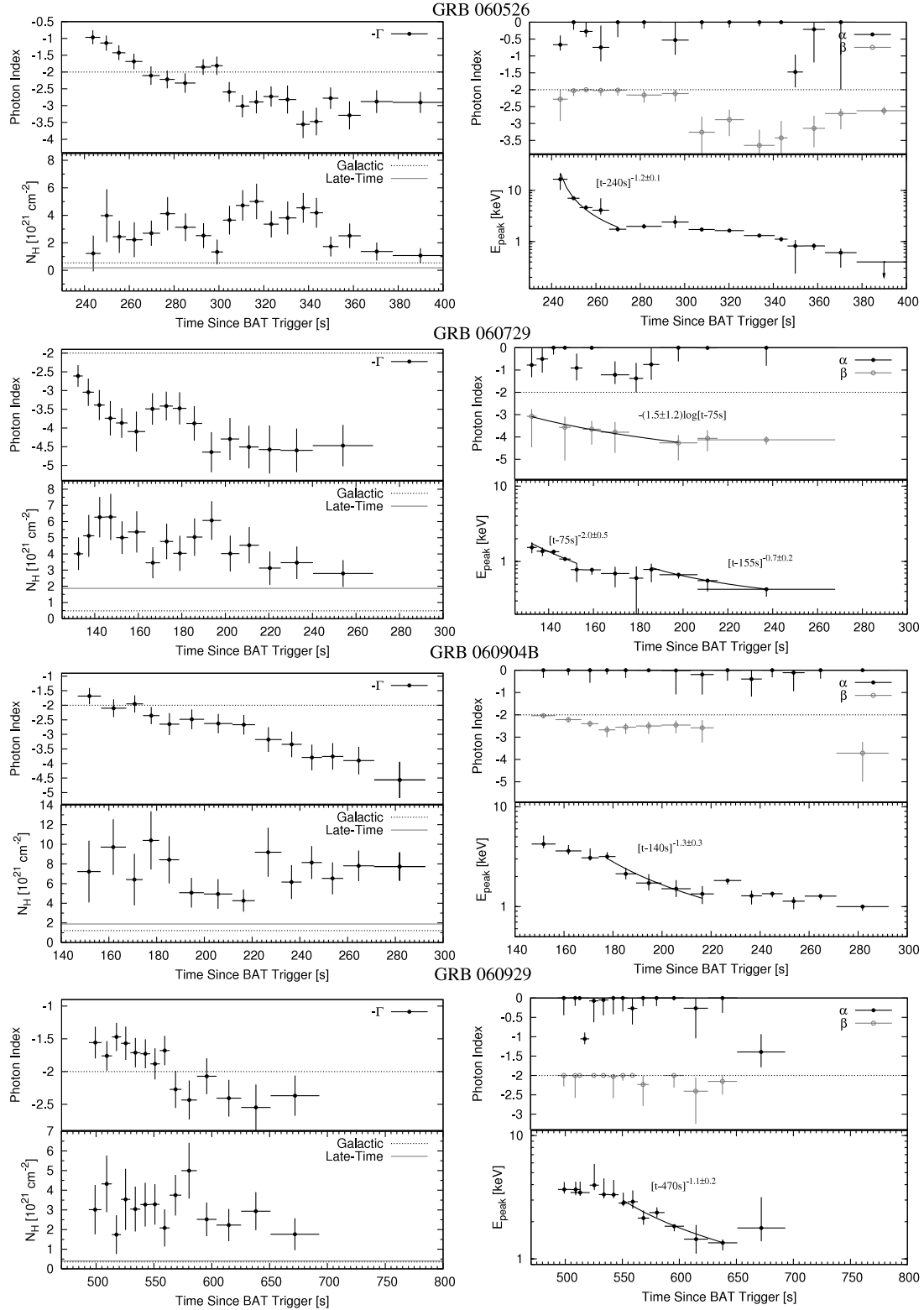
FIG. 8.— Power-law (*left*) and Band model (*right*) fits to the GRBs 060526, 060729, 060904B, and 060929. Time-correlated N_H-Γ variations in the left plots are fit by spectral models with time-evolving E_{peak} values in the right plots. Trends in the Band model parameters, when observed, are fitted and presented in Table 3 and in the text. See also Fig. 3. In the Band model plots, α-values that appear to be above and outside the plotted range are those that reach and remain at the parameter bound $\alpha = 0$ (see § 3.1). [*See the electronic edition of the Journal for a color version of this figure.*]
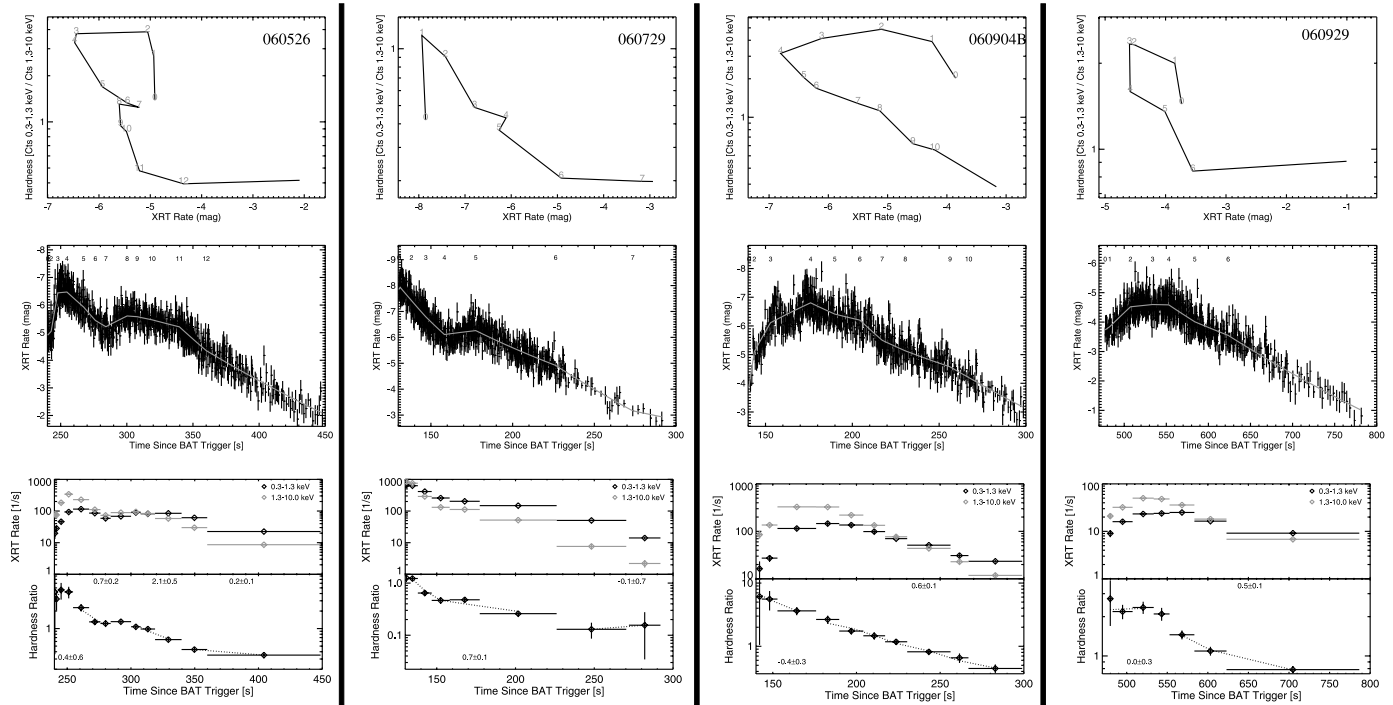
Fig. 9.—*Top*: Hardness plots for GRBs 060526, 060729, 060904B, and 060929. *Middle*: Hardness vs. rate fits, indexed as a function of time, showing evolution along roughly parallel tracks. *Bottom*: X-ray light curve and fit as source of the time indexing. The X-ray light curve in each band for each time segment and the hardness during each time segment is shown. This hardness is well fit during the declines by the rate to a power close to 0.5. See also Fig. 6. [*See the electronic edition of the Journal for a color version of this figure.*]

The typical $E_{\rm peak}$ values for the XRT are 2 orders of magnitude below the mode of the BATSE distribution (Preece et al. 2000; Kaneko et al. 2006). As we discuss below, some of the soft $E_{\rm peak}$ values may be due to viewing effects of delayed emission with an intrinsically higher $E_{\rm peak}$. However, the soft flare emission implies intrinsic spectral evolution or soft late central engine activity, which would extend the BATSE $E_{\rm peak}$ distribution. Our derived values for α are poorly constrained, but likely consistent with the BATSE distribution. Finally, it is remarkable that very soft emission is observed in a few cases, extending the distribution in β to very low values < -6 (Figs. 8 and 10; GRBs 050714B and 050822, as discussed in Paper I).

5.4. *Interpretation of the Spectral Variations*

Although intrinsic spectral evolution is likely also present, most of the softening trend and hardness-intensity correlation in GRB pulses is attributed to the so called curvature effect (Fenimore et al. 1996; Sari & Piran 1997; Norris 2002; Ryde & Petrosian 2002; Kocevski et al. 2003; Qin et al. 2004; Qin & Lu 2005; Shen et al. 2005). This is also the widely accepted explanation for the rapid-decline X-ray tails of the prompt emission
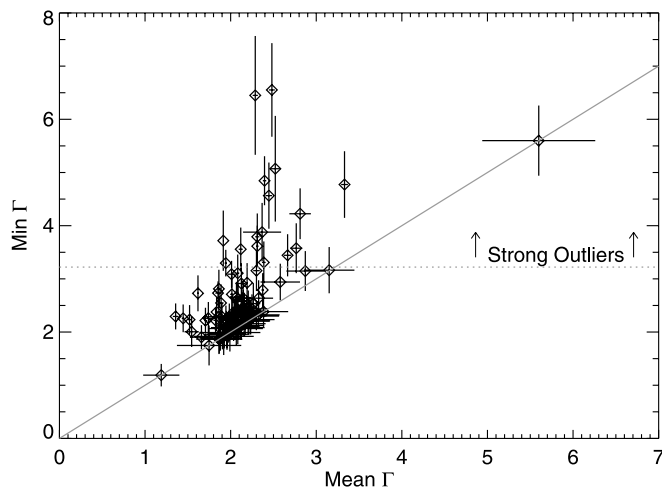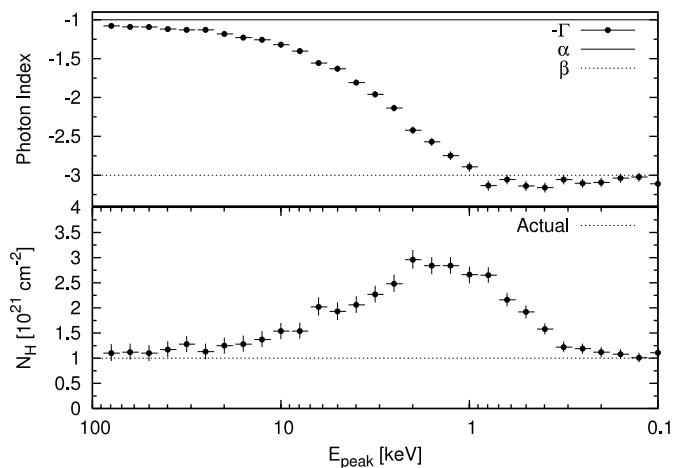

Fig. 10.—As also discussed in Paper I, an outlier population of very soft *Swift* XRT afterglow time regions with respect to the majority population clustering near photon index $\Gamma \sim 2$. [*See the electronic edition of the Journal for a color version of this figure.*]

Fig. 11.—Power-law fits to high signal-to-noise ratio (S/N) data (10^4 counts, 0.3–10.0 keV) simulated from a Band spectral model with $\alpha = -1$ and $\beta = -3$. Each fit is statistically acceptable ($\chi^2/\nu \sim 1$). With the passage of the νF_ν peak-energy $E_{\rm peak}$ values, the best-fit photon index Γ steepens smoothly. An artificial increase in the inferred X-ray column density $N_{\rm H}$ linearly proportional to Γ is observed for peak energies $E_{\rm peak}$ in the XRT bandpass. The effect is present, with larger $N_{\rm H}$ error bars, for spectra with few counts. [*See the electronic edition of the Journal for a color version of this figure.*]
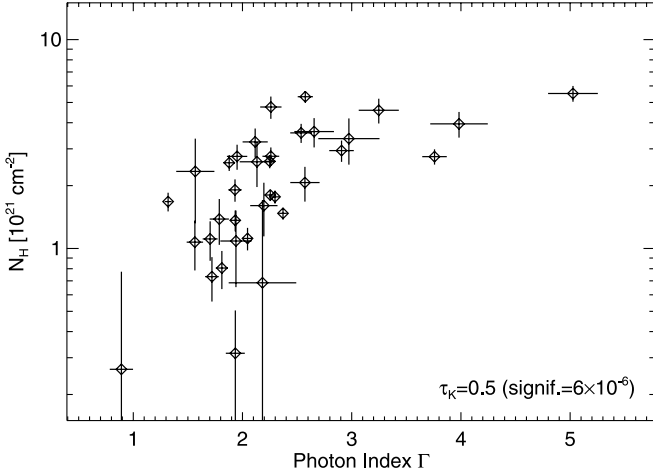
Fig. 12.—Time-integrated spectral fits to the flares in Table 2, also shown in Fig. 13, demonstrating a significant positive correlation between the column density parameter N_H (observed minus Galactic) and the photon index Γ. Although these quantities are correlated for a given spectrum, we do not expect a correlation at different times for the same event (see below) or at any time for separate events as found here. This is evidence relating the X-ray flares to an excess spectral curvature at X-ray wavelengths.

TABLE 2
27 BRIGHT XRT FLARES

GRB	Time Region (s)	GRB	Time Region (s)
050502B..............	400–1200	050712..................	150–300
050730................	130–300	050730..................	300–600
050730................	600–800	050822..................	410–650
050904..............	350–600	051117A..............	1250–1725
051117A..............	800–1250	060111A..............	200–500
060124..............	300–650	060124..................	650–900
060204B..............	100–270	060204B..............	270–450
060210................	100–165	060210..................	165–300
060210................	350–450	060418..................	83–110
060607A..............	93–130	060607A..............	220–400
060714..............	100–125	060714..................	125–160
060714..............	160–230	060729..................	156–300
060904A..............	250–600	060904A..............	600–1000
060904B..............	140–300		

(Nousek et al. 2006; Zhang et al. 2006a; Panaitescu 2007). Derivations from first principles of the curvature effect on the observed spectra can be found in Granot et al. (1999) and Woods & Loeb (1999).

If we imagine a spherical emitting shell at radius R that emits as a delta function at t_0, the spectral flux F_E scales with the Doppler factor δ as $F_E \propto F_E(E\delta)/\delta^2$, where $\delta \equiv \gamma(1 - \beta_c \cos\theta)/(1 - \beta_c) \approx 1 + \gamma^2\theta^2$ and θ is the viewing angle to the emitting material off the line of sight. The photons from larger angles will be delayed in time, $t - t_0 = (1+z)(\delta-1)(1-\beta_c)R/(c\beta_c) \approx (1+z)\theta^2 R/(2c) \propto \delta$.

For a power-law spectrum $F_E \propto E^{1-|\alpha|}$, the observed flux declines in time as a power law $(t - t_0)^{-|b|}$, with $|b| = 1 + |\alpha|$ and no hardness evolution (Kumar & Panaitescu 2000). For a Band spectrum, we see either the low energy index α or the high energy index β or some average of the two, depending on the location of E_{peak} with respect to the bandpass. E_{peak} will decline as $(t - t_0)^{-1}$. When E_{peak} is in the band, the νF_ν turnover implies

$-\alpha_{eff} \approx 1$–2, and we expect to see a power-law hardness-intensity correlation $E_{peak} \propto F^{0.3}$–$F^{0.5}$. Larger values of the index are favored observationally, because they correspond to a higher flux. We will observe the hardness (which our simulations show to scale linearly with E_{peak} for a range of Band model parameters) to approximately linearly correlate with the fluence. Departures from this expected behavior will occur for emitting shells of different shape, for an inhomogeneous emitting surface, for non-instantaneous emission, or if intrinsic spectral evolution dominates. Also, the measured flux decay in time is a strong function of the assumed t_0 (e.g., Liang et al. 2006).

Our best-fit HR-F relation index (Fig. 13) and our average E_{peak}-F relation index (§ 5.3; Table 3) are consistent with those expected in this simple picture. Spectral variations are not inconsistent with the curvature effect, as recently suggested by Zhang et al. (2006b). Rather, they facilitate a higher order test of the curvature effect and allow us to confirm the curvature effect in a way that shows the X-ray phenomenology to closely parallel the γ-ray phenomenology. Moreover, the scatter in our HR-F relation (Fig. 13, *left*) is less than that found for time index–energy index relations (Nousek et al. 2006; Panaitescu 2007), which assume power-law X-ray spectra.

The mean time index for the E_{peak} decays in Table 3 is -1.4 ± 0.6, consistent with unity. This indicates that our choice to associate t_0 with the start of the flare or pulse is roughly correct, in agreement with the findings of Liang et al. (2006). Although we see evidence that later flares often have lower E_{peak} in the same event with multiple flares (e.g., Fig. 3), we do not see a correlation between t_0 in Table 3 and E_{peak} just after that time.
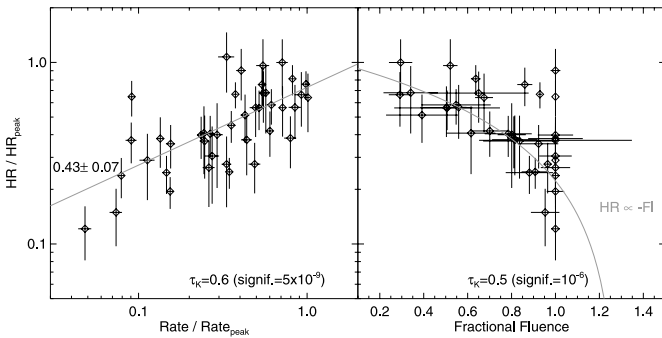

Fig. 13.—*Left*: During the decline phase of the X-ray flares from Table 2 (also Fig. 12), the hardness ratio (HR), defined as the ratio of counts in the 1.3–10.0 keV band to the counts in the 0.3–1.3 keV band, correlating strongly (Kendall's $\tau_K = 0.6$) with the count rate (0.3–10.0 keV), following roughly a power-law relationship. There is a consistent and long-known relation valid for a majority of pulses seen in GRBs (Golenetskii et al. 1983; Kargatis et al. 1995; Ford et al. 1995; Borgonovo & Ryde 2001). *Right*: Hardness also correlating strongly with the fluence (*right*), as is also the case for GRBs (Liang & Kargatis 1996; Ryde 2005). That is, the hardness evolves more rapidly when the flares are brighter. [*See the electronic edition of the Journal for a color version of this figure.*]
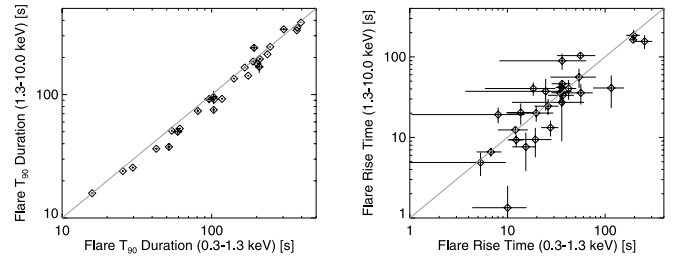

Fig. 14.—Timing statistics for the bright flares in (Table 2). The flare T_{90} durations (*left*) and rise times (*right*) are systematically longer in the soft X-ray channel (*left*), by $8\% \pm 1\%$ and $25\% \pm 5\%$, respectively. Norris et al. (1996) and Fenimore et al. (1995, 1996) discuss similar properties of GRB pulses. [*See the electronic edition of the Journal for a color version of this figure.*]
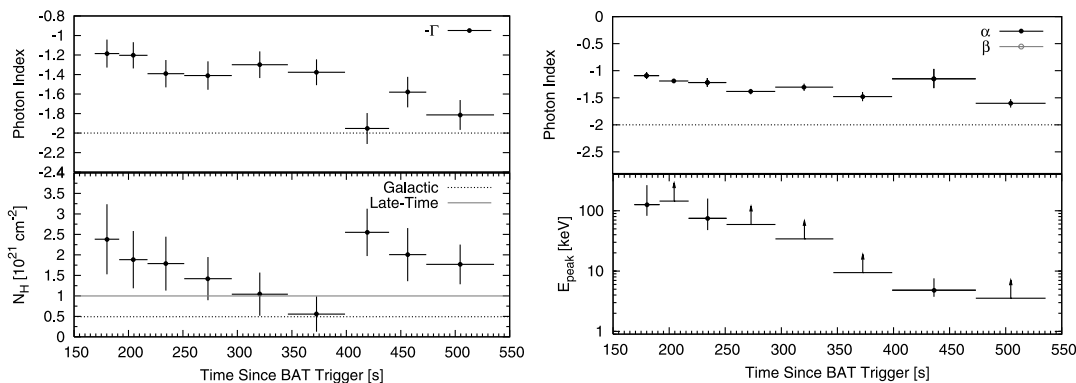
Fig. 15.— Variation in N_H. We believe N_H variations are an incorrect explanation for the spectral evolution in the flaring, high-z GRB 050904. These data are coarsely grouped into three time intervals by Campana et al. (2007) and fit to show a time-decreasing X-ray column density. At finer time resolution (*left*), we see that the N_H parameter decreases toward the late-time value before and after an unphysical increase. The maximum N_H corresponds to E_{peak} values in the XRT band (*right*). The hardness during this period tracks the flux to the 0.6 ± 0.2 power (see also Butler & Kocevski 2007), consistent with a Band model spectrum evolving via the curvature effect (§ 5.4). [*See the electronic edition of the Journal for a color version of this figure.*]

We have observed two cases of α evolution (Fig. 3, *right*), which accompanies the E_{peak} evolution. Due to the proximity of E_{peak} to the bottom of the XRT passband and also due to the possibility of a modestly incorrectly measured N_H, these cases should be interpreted cautiously. This evolution, or that observed for β (§ 5.3), cannot be accounted for by the curvature effect and must be intrinsic.

In most cases, the X-ray light curve is simply declining early on (possibly with weak flaring superimposed), and we observe approximately secularly declining E_{peak} and HR values. In a handful of cases where multiple flares follow a GRB (e.g., Fig. 6, 060124; Fig. 7, 060714), the hardness tracks the flux both upward and downward. Because the brightest case (060124 in Fig. 3, *right*) also shows upward and downward E_{peak} trends, we believe this behavior is likely responsible for the HR evolution. The parallel or overlapping tracks observed here for bursts with multiple flares on the HR-F diagram are also seen for GRB pulses (Borgonovo & Ryde 2001).

6. CONCLUSIONS

We have measured the spectral evolution properties for GRBs and afterglows in the *Swift* sample, taken prior to and including GRB 061210. We have established similar spectral evolution properties for the X-ray emission coincident with two GRBs

(060124 and 061121) and the X-ray emission in the rapid declines following several GRBs and in 27 flares occurring 10^2–10^3 s after their GRBs.

Indirectly, from absorbed power-law fits that show a time-variable N_H, and directly, from Band model fits, we have derived constraints on the νF_ν spectrum peak-energy E_{peak}. We observe this quantity to evolve in time and to typically cross the XRT bandpass during the early X-ray afterglow. Because the X-ray hardness changes little for Band spectra with E_{peak} outside the bandpass, the strong hardness variation we observe in >90% of *Swift* early afterglows (Butler & Kocevski 2007) implies $E_{peak} \approx$ 1 keV, typically. We observe this evolution in data taken in both the WT and PC modes (e.g., 050607 and 050714B) and following both long duration and short duration (e.g., 050724 and 051227) GRBs. The hardness ratio and E_{peak} values scale with the flux, as would be expected from the relativistic viewing effects of an expanding fireball. This implies that the true variability timescale is *even shorter* than that measured from the observed flare durations.

Because the late flares are typically softer than the GRB emission and because the Band model α and β parameters also appear to evolve in some cases, there is likely an intrinsic evolution of the fireball. If the flares are due to shells moving out with lower bulk Lorentz factor or at larger radii than for the prompt emission, we may expect to see differences in the time properties of flares observed at different epochs. This will be explored in a separate paper (Kocevski et al. 2007). If the evolution is occurring on a longer timescale at later times, when the sensitive XRT is observing, the early X-ray afterglows would provide a unique testbed for theories explaining GRBs, the emission mechanisms, and possibly the progenitors. The internal shocks must be active after 10^3 s and must be able to produce emission with $E_{peak} \approx$ 1 keV and very soft $\beta \lesssim -6$ (see also Zhang et al. 2006a). Especially relevant to the Gamma-ray Large Area Telescope (GLAST), electrons energized by the X-ray flares may Compton-upscatter photons at larger radii or in the external shock to the γ-rays (Wang et al. 2006).

TABLE 3
E_{peak} Evolution Properties

GRB	t_0 (s)	Time Index	Flux Index	Data Points Fit
060124	510	-2.9 ± 1.3	-3.6 ± 1.7	2
060124	555	-2.2 ± 0.3	-1.8 ± 0.5	3
060124	567	-0.8 ± 0.1	-0.3 ± 0.1	4
060124	685	-2.2 ± 0.4	-1.2 ± 0.2	3
060526	240	-1.2 ± 0.1	-1.0 ± 0.1	5
060614	0	-2.1 ± 0.1	-0.72 ± 0.03	19
060729	75	-2.0 ± 0.5	-0.4 ± 0.1	5
060729	155	-0.7 ± 0.2	-0.4 ± 0.1	4
060904B	140	-1.3 ± 0.3	-0.7 ± 0.2	5
060929	470	-1.1 ± 0.2	-0.6 ± 0.1	7

Notes.—Changes in the best-fit E_{peak} with time are relative to the start t_0. The start time is somewhat arbitrary, based on the approximate start of each pulse (or flare).

REFERENCES

Band, D. L., et al. 1993, ApJ, 413, 281
Barthelmy, S. D., et al. 2005, Nature, 438, 994
Borgonovo, L., & Ryde, F. 2001, ApJ, 548, 770
Burrows, D. N., et al. 2005a, Science, 309, 1833
———. 2005b, Space Sci. Rev., 120, 165
Butler, N. R. 2007a, ApJ, 656, 1001 (Paper I)
———. 2007b, AJ, 133, 1027
Butler, N. R., & Kocevski, D. 2007, ApJ, submitted (astro-ph/0702638)
Campana, S., et al. 2006a, Nature, 442, 1008
———. 2006b, GCN Circ. 5162
———. 2007, ApJ, 657, L17
Cusumano, G., et al. 2006, Nature, 440, 164
Dickey, J. M., & Lockman, F. J. 1990, ARA&A, 28, 215
Falcone, A., et al. 2006, ApJ, 641, 1010
Fan, Y. Z., & Wei, D. M. 2005, MNRAS, 364, L42
Fenimore, E. E., Madras, C. D., & Hayakshin, S. 1996, ApJ, 473, 998
Fenimore, E. E., et al. 1995, ApJ, 448, L101
Fishman, G. J., et al. 1989, in Proc. GRO Science Workshop (Greenbelt: NASA GSFC), 2
Ford, L. A., et al. 1995, ApJ, 439, 307
Frontera, F., et al. 2000, ApJS, 127, 59
Gehrels, N., et al. 2004, ApJ, 611, 1005
———. 2006, GCN Circ. 5839
Golenetskii, S. V., et al. 1983, Nature, 306, 451
Granot, J., Piran, T., & Sari, R. 1999, ApJ, 513, 679
Grupe, D., et al. 2006a, GCN Circ. 5365
———. 2006b, GCN Circ. 5505
Holland, S. T., et al. 2006, GCN Circ. 4570
Ioka, K., et al. 2005, ApJ, 631, 429
Kaneko, Y., et al. 2006, ApJS, 166, 298
Kargatis, V. E., et al. 1995, Ap&SS, 231, 177
Kocevski, D., Butler, N. R., & Bloom, J. S. 2007, ApJ, submitted (astro-ph/0702452)
Kocevski, D., Ryde, F., & Liang, E. 2003, ApJ, 596, 389
Krimm, H. A., et al. 2006, GCN Circ. 5311
Kumar, P., & Panaitescu, A. 2000, ApJ, 541, L51
Lazzati, D., & Begelman, M. C. 2006, ApJ, 641, 972
Liang, E., & Kargatis, V. 1996, Nature, 381, 49
Liang, E. W., et al. 2006, ApJ, 646, 351

Markwardt, C. B., et al. 2006, GCN Circ. 5654
Morreti, A., et al. 2006, A&A, 451, 777
Norris, J. P. 2002, ApJ, 579, 386
Norris, J. P., et al. 1996, ApJ, 459, 393
Nousek, J. A., et al. 2006, ApJ, 642, 389
O'Brien, D. P., et al. 2006, ApJ, 647, 1213
Pagani, C., et al. 2006, ApJ, 645, 1315
Page, K. L., et al. 2006, GCN Circ. 5823
———. 2007, ApJ, in press (astro-ph07041609)
Panaitescu, A. 2007, MNRAS, in press (astro-ph/0612170)
Panaitescu, A., et al. 2006, MNRAS, 366, 1357
Parsons, A. M., et al. 2006, GCN Circ. 5252
Preece, R. D., Briggs, M. S., Mallozzi, R. S., Pendleton, G. N., Paciesas, W. S., & Band, D. L. 2000, ApJS, 126, 19
Protassov, R., et al. 2002, ApJ, 571, 545
Qin, Y.-P., & Lu, R. J. 2005, MNRAS, 362, 1085
Qin, Y.-P., et al. 2004, ApJ, 617, 439
Rees, M. J., & Mészáros, P. 1994, ApJ, 430, L93
Rol, E., et al. 2007, MNRAS, 374, 1078
Romano, P., et al. 2006a, A&A, 450, 59
———. 2006b, A&A, 456, 917
Ryde, F. 2005, A&A, 429, 869
Ryde, F., & Petrosian, V. 2002, ApJ, 578, 290
Sakamoto, T., et al. 2004, ApJ, 602, 875
Sari, P., & Piran, T. 1997, ApJ, 485, 270
Sari, R., Piran, T., & Narayan, R. 1998, ApJ, 497, L17
Scargle, J. D. 1998, ApJ, 504, 405
Shen, R. F., Song, L. M., & Li, Z. 2005, MNRAS, 362, 59
Starling, R. L. C., et al. 2005, A&A, 442, L21
Tagliaferri, G., et al. 2005, Nature, 436, 985
Vaughan, S., et al. 2006, ApJ, 638, 920
Wang, X.-Y., Li, Z., & Mészáros, P. 2006, ApJ, 641, L89
Wijers, R. A. M. J., & Galama, T. J. 1999, ApJ, 523, 177
Willingale, R., et al. 2006, ApJ, submitted (astro-ph/0612031)
Woods, E., & Loeb, A. 1999, ApJ, 523, 187
Yamazaki, R., et al. 2006, MNRAS, 369, 311
Zhang, B., Fan, Y. Z., Dyks, J., Kobayashi, S., Mészáros, P., Burrows, D. N., Nousek, J. A., & Gehrels, N. 2006a, ApJ, 642, 354
Zhang, B.-B., Liang, E.-W., & Zhang, B. 2006b, ApJ, in press (astro-ph/0612246)